

# LiMn<sub>x</sub>Fe<sub>1-x</sub>PO<sub>4</sub> Anodefree Batteries: A Scalable, Low Cost, Energy Dense Lithium Cell Design

Gerard Bree,\* Daniela Proprentner, Galo Paez-Fajardo, Veronika Majherova, Eleni Fiamegkou, and Louis Piper\*

The anodefree (AF) configuration of lithium batteries represents a low-cost, high energy density alternative to current generation chemistries, and coupling with Ni and Co-free LiMn<sub>x</sub>Fe<sub>1-x</sub>PO<sub>4</sub> (LMFP) cathodes further reinforces these advantages. In this work, this cell type in coin and pouch format is manufactured and evaluated, establishing key performance characteristics and optimized test protocols, while identifying outstanding challenges limiting cell lifetime. The AF LMFP coin cell provides a 35% stack-level energy density advantage over a traditional full cell

(with graphite anode) when using a 60:40 Mn:Fe LMFP variant, which improves to a 42% advantage when Mn content was increased to 80% (at the cost of more rapid capacity loss). Cycling over the potential range of 3.0–4.5 V maximizes cell lifetime, while the dominant degradation mechanism is identified as irreversible Li loss associated with a disadvantageous evolution in plated Li morphology. Finally, the AF battery manufacturing is scaled to large-area pouch format to demonstrate commercial viability and compatibility with current industrial processes.

## 1. Introduction

Next generation lithium-ion battery chemistries of all varieties offer some potential gain to either cell energy density, cost, or safety (often some combination of all three). Lithium metal represents the “holy-grail” of lithium-ion battery anodes, possessing extremely high gravimetric (3860 mAh g<sup>-1</sup>) and volumetric (2061 mAh cm<sup>-3</sup>) capacities, coupled with a low electrochemical potential of  $-3.04$  V versus SHE.<sup>[1]</sup> It thus offers substantial advantages over widely used graphite anodes (372 mAh g<sup>-1</sup>). However, Li anodes have not yet found commercial usage in rechargeable battery systems, due to several challenges. First, thin lithium films (<50 µm), required for high volumetric density, are difficult to manufacture at high levels of purity in a cost effective manner, particularly as the high reactivity necessitates special handling considerations.<sup>[2]</sup> Second, the reversibility of the lithium plating

and stripping process during cell operation is not as efficient as (de)intercalation from/into graphite, and thus the lifetime of Li-metal cells has thus far been comparatively limited. Finally, Li tends to plate quite nonuniformly, forming dendrites which in extreme cases can short-circuit active cells, generating substantial heat and posing a fire safety risk.<sup>[3]</sup>

The so-called “anodefree” (AF) or “anodeless” cell configuration neatly overcomes the first of these challenges through simply manufacturing the cell without elemental Li present in the pristine state, relying entirely on the lithium initially present in the cathode (in the same manner as a standard graphite-containing cell).<sup>[4]</sup> In the AF cell, the pristine “anode” consists solely of a current collector, typically copper foil. During operation, the cell behaves as a Li-metal cell (involving plating and stripping of Li), and thus AF cells are often referred to as “zero-excess” Li-metal cells. This dramatic simplification of the manufacturing process reduces costs compared with both conventional “full” cells and Li-metal cells. This comes at a cost, however, the “zero-excess” nature of the AF cell type means that any Li inventory loss suffered cannot be replenished and will directly and immediately impact cell capacity. It should be noted that this is the case in traditional cells with graphite anodes (which achieve long lifetimes), however Li anodes typically undergo more rapid inventory loss and thus shorter lifetimes are common, often <100 cycles. The challenge of improving Li plating morphology to slow inventory loss and prevent dendrite-related shorting remains. Many cathode materials have been trialed in the AF cell format, and a wide variety of lifetime-improvement strategies have been evaluated (Table 1). These strategies include electrolyte formulation screening, formation/test protocol optimization and modification of the anode current collector, all with the goal of improving Li plating morphology and reducing the rate of inventory loss. Stack pressure during cell operation is known to be a particularly

G. Bree, D. Proprentner, G. Paez-Fajardo, V. Majherova, E. Fiamegkou,  
L. Piper  
Warwick Manufacturing Group  
University of Warwick  
Coventry CV4 7 AL, UK  
E-mail: Gerard.bree@warwick.ac.uk  
Louis.piper@warwick.ac.uk

G. Bree, D. Proprentner, G. Paez-Fajardo, V. Majherova, E. Fiamegkou,  
L. Piper  
The Faraday Institution  
Quad One  
Harwell Science and Innovation Campus  
Didcot OX11 0RA, UK

 Supporting information for this article is available on the WWW under <https://doi.org/10.1002/batt.202500507>

 © 2025 The Author(s). *Batteries & Supercaps* published by Wiley-VCH GmbH. This is an open access article under the terms of the Creative Commons Attribution License, which permits use, distribution and reproduction in any medium, provided the original work is properly cited.

Ref.	Cathode	Cell format	Electrolyte	Lifetime (cycles >80% performance)	Themes
[35]	NMC532	Pouch	LiBF4 + LiDFOB in FEC:DEC	90	Electrolyte development
[5]	NMC532	Pouch	1 m LiPF6 in 1:2 FEC:TFEC	40	Stack pressure optimization
[13]	NMC532	Pouch	LiBF4 + LiDFOB in FEC:DEC	80	Evaluation of various cathodes, depth of discharge optimization
	NMC811	Pouch		60	
	LCO	Pouch		55	
	LFP	Pouch		20	
[36]	LFP	Coin	LHCE, LiFSI:TMS:TTE = 1:3:3	150	Cathode prelithiation additive
[14]	LFP	Coin	2 m LiFSI in 1,3-dioxolane (DOL) with 0.5 m LiNO3 additive	50	Pulse charging
[37]	NMC811	Coin	1 m LiPF6 in EC:DMC (1:1 vol%) with 5 vol% FEC	30	Highly fluorinated electrolyte
[34]	NMC811	Coin	LiBF4 + LiDFOB in FEC:DEC	25	Formation optimization
[38]	LFP	Pouch	1.0 m LiTFSI in DME:DOL (1:1 vol), 5 wt% LiNO3	190	Anode artificial SEI, cathode prelithiation additive
[19]	LMFP	Swagelok	4 m LiFSI in DME, Ionic liquid additive	60	Electrolyte development
	NMC613	Swagelok		140	
[20]	LMFP	Coin	Gel polymer	10	Electrolyte development, porous LMFP
[39]	LNMO	Coin	4.5 m LiFSI in Py13FSI	120	Si-PAN coated Cu foil
[40]	LNMO	Pouch	7 m LiFSI in FEC	>50	Cathode chemical/electrochemical prelithiation

key factor,<sup>[5]</sup> whereby traditional coin cells underperform relative to pouch cells due to low and inhomogeneous pressure,<sup>[6]</sup> reinforcing the need for performance evaluation in larger, more industrially-relevant cell formats.

Aligned with the goal of reducing cell cost, olivine phosphate-based cathodes, most commonly lithium iron phosphate (LiFePO<sub>4</sub>, LFP), have undergone a renaissance in electric vehicles battery systems in recent years.<sup>[7,8]</sup> This is attributed to the high system-level energy density now achievable through the use of larger cells and direct cell-to-pack technology, enabled by the excellent safety characteristics of phosphate cells.<sup>[9,10]</sup> The lower cost compared with layered oxides, e.g., LiNi<sub>x</sub>Mn<sub>y</sub>Co<sub>z</sub>O<sub>2</sub> (NMC), relies on the elimination of rare and costly Co and Ni from the structure, both now listed as critical raw materials in the EU and US.<sup>[11,12]</sup> The LFP AF configuration has thus been identified and investigated as an advantageous low-cost system,<sup>[13–15]</sup> however the lower specific capacity and output voltage of LFP means that the energy density of this design still lags behind NMC\Graphite systems. Replacing some of the Fe in LFP with Mn, forming LiMn<sub>x</sub>Fe<sub>1-x</sub>PO<sub>4</sub> (LMFP), offers a potential 20% energy density advantage due to the higher discharge potential of the Mn<sup>2+/3+</sup> redox couple, while maintaining excellent stability and safety characteristics, and this material has recently been commercialized in full cell format.<sup>[8,16–18]</sup> The AF LMFP cell configuration thus offers unique potential as a low-cost, highly scalable, and energy dense system, however has not yet been studied in depth, with only two reports involving limited cell formats from literature identified.<sup>[19,20]</sup> The move from LFP to LMFP may also be expected to pose additional cell lifetime and kinetic challenges due to Mn dissolution and Jahn-Teller distortion, however to date, these have only been identified for the full cell system,<sup>[21,22]</sup>

and their effect on AF cell performance is unknown. Establishing the key performance characteristics, degradation mechanisms and optimized cycling protocols is necessary for a full evaluation of this promising cell format.

In this work, we combine the latest developments in LMFP and AF cell technologies, manufacturing coin and large-area pouch cells to evaluate performance and develop a set of optimized formation and cycling protocols enabling maximum cell lifetime. The novel cell format provides a large 35% boost to stack-level energy density over a similar full cell with graphite anode. Through ex-situ morphological and chemical analysis linked with DVA of LMFP AF coin cells, Li loss associated with disadvantageous plating morphology is identified as the major degradation mechanism. Both upper and lower cutoff voltages (UCV and LCV) are shown to dramatically impact capacity loss, and optimized protocols are established. LMFP is benchmarked against conventional LFP and a high-Mn content variant is trialed to further increase energy density. Finally, a large-area commercial-style pouch cell is manufactured to showcase scalability and ease of manufacture.

## 2. Results and Discussion

The potential advantage of the AF cell system over those involving traditional anode materials lies in the step change in achievable energy density (both gravimetric and volumetric). To evaluate and illustrate this in the context of LMFP cathodes, coin cells were assembled in both the AF and “full” cell LMFP configurations (using a high cathode coat weight of 135 gsm and a high active material content of 93%). Figure 1a shows schematics of

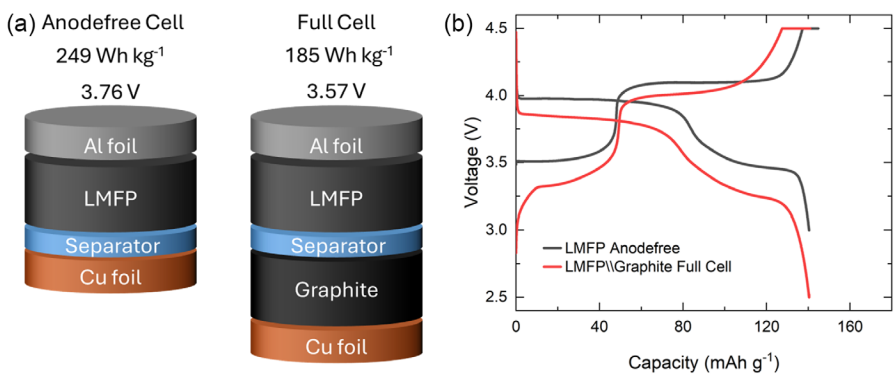


**Figure 1.** a) Schematic and b) voltage profile during 1st postformation cycle, comparing the LMFP AF and full cell configurations in coin cell format. Gravimetric energy density values are calculated based on dry stack mass. More details on the parameters and calculations are provided in the SI.

these configurations, whereby the removal of the graphite provides savings to both weight and volume. Figure 1b shows voltage profiles during the first postformation cycle (i.e., cycle 3) of both cells. Here, optimized cycling protocols were utilized for both cell types; the AF cell was cycled at a rate of C/10, D/3 over the range 3.0–4.5 V, mirroring the slow charge, fast discharge, and reduced depth-of-discharge protocols established as optimum for similar AF NMC cells.<sup>[23]</sup> The full cell was cycled using a conventional symmetric C/3 protocol over the range 2.5–4.5 V. Both cells utilized a constant voltage step at top of charge. The dual plateau nature of LMFP is clearly visible. While the cells achieved identical discharge capacities of 140 mAh g<sup>-1</sup>, the AF cell exhibited a higher mean discharge voltage of 3.76 V (compared with 3.59 V for the full cell), which can be attributed to the lower potential of the Li anode compared with graphite. This boost to average discharge voltage provides an energy density advantage in addition to that gained from the removal of anode mass. Through consideration of the “stack” mass (including active layers, current collecting foils, and separator), it was calculated that the AF and full cells provided stack-level gravimetric energy densities of 249 and 185 Wh kg<sup>-1</sup>, respectively, a 35% advantage.

The electrochemical processes at play within the LMFP AF cell were further examined via a 3-electrode cell configuration utilizing a Li reference electrode, enabling monitoring of individual cathode and anode potentials during charge-discharge. Figure 2a shows the evolution in these potentials during the first formation cycle, performed at a rate of C/10 charge and C/3 discharge. The cathode exhibited clear charge voltage plateaus associated with the oxidation of Fe ( $2^+ \rightarrow 3^+$ ) at  $\approx 3.5$  V versus Li<sup>+</sup>/Li and subsequently Mn ( $2^+ \rightarrow 3^+$ ) at  $\approx 4.1$  V versus Li<sup>+</sup>/Li, and the cell voltage closely follows that of the cathode. The cell exhibited a high charge capacity of 163 mAh g<sup>-1</sup> (close to the theoretical value for LMFP, 170 mAh g<sup>-1</sup>), while discharge capacity was 143 mAh g<sup>-1</sup>. Through the use of the 3-electrode cell, it can be observed that the first discharge capacity is in fact cathode-limited, whereby the rapid fall in cell potential toward the end of discharge tracks that of the cathode, at which time the anode potential is still  $< 30$  mV, indicating the presence of remaining cyclable Li on the Cu. Figure 2b shows a zoomed plot of the anode potential evolution during the first charge cycle.

Upon the initial application of a charge current, the anode potential quickly dropped to  $< 0$  V versus Li<sup>+</sup>/Li as Li was first plated onto the Cu foil. A nucleation overpotential of  $\approx 11.8$  mV was sufficient to drive nucleation of Li on the lithiophobic Cu surface. Subsequently, the overpotential fell as more Li sites became available, with the plating overpotential reaching  $\approx 5$  mV at the end of charge. Figure 2c shows the profiles during cycle 2. Here the anode potential increased rapidly at the end of discharge (reaching 0.237 V vs. Li<sup>+</sup>/Li), indicating both the complete removal of cyclable Li from the Cu surface, and that the capacity was limited by Li inventory (which remains the case from that point on, Figure S1, Supporting Information). The 3-electrode configuration also enabled the identification of peaks in differential voltage analysis (DVA) of a discharge (Figure 2d), whereby the cathode peak at 83 mAh g<sup>-1</sup> corresponds to the transition from Mn redox to Fe redox. The anode DVA curve shows little activity as no phase transitions are expected on this electrode.

LMFP is most often benchmarked against its parent olivine cathode, LFP,<sup>[24–26]</sup> as the latter material has been widely studied in academia and industry and thus exhibits well-understood characteristics. Here, AF LMFP and LFP coin cells were assembled and subjected to repeated charge–discharge cycling (Figure 3a). The voltage ranges were chosen to encompass the full electrochemical activity of the materials, i.e., 3.0–4.4 V for LMFP and 3.0–4.0 V for LFP. In addition, an identical LFP cell was cycled at 3.0–4.4 V to provide a like-for-like comparison with LMFP. A cycling duration of 50 cycles was sufficient to showcase substantial differences between materials. Remarkably, the LMFP cell demonstrated far greater capacity retention than either LFP cell. The varying stability was linked with differences in coulombic efficiency, whereby at, e.g., cycle 6, LMFP was 97.5% and the LFP cells were  $\approx 94.2\%$ . These findings are in dramatic opposition to conventional knowledge regarding these phosphate materials, whereby LMFP is typically considered a less stable material due to the occurrence of Mn dissolution and its subsequent deposition on the anode, where it induces significant lithium inventory loss.<sup>[26–28]</sup> While the poor stability of the LFP AF cells here is notable and warrants further study, similar cells have shown relatively poor performance in previous reports, attributed to incompatibility with some carbonate electrolyte systems.<sup>[13,29,30]</sup> Nevertheless,

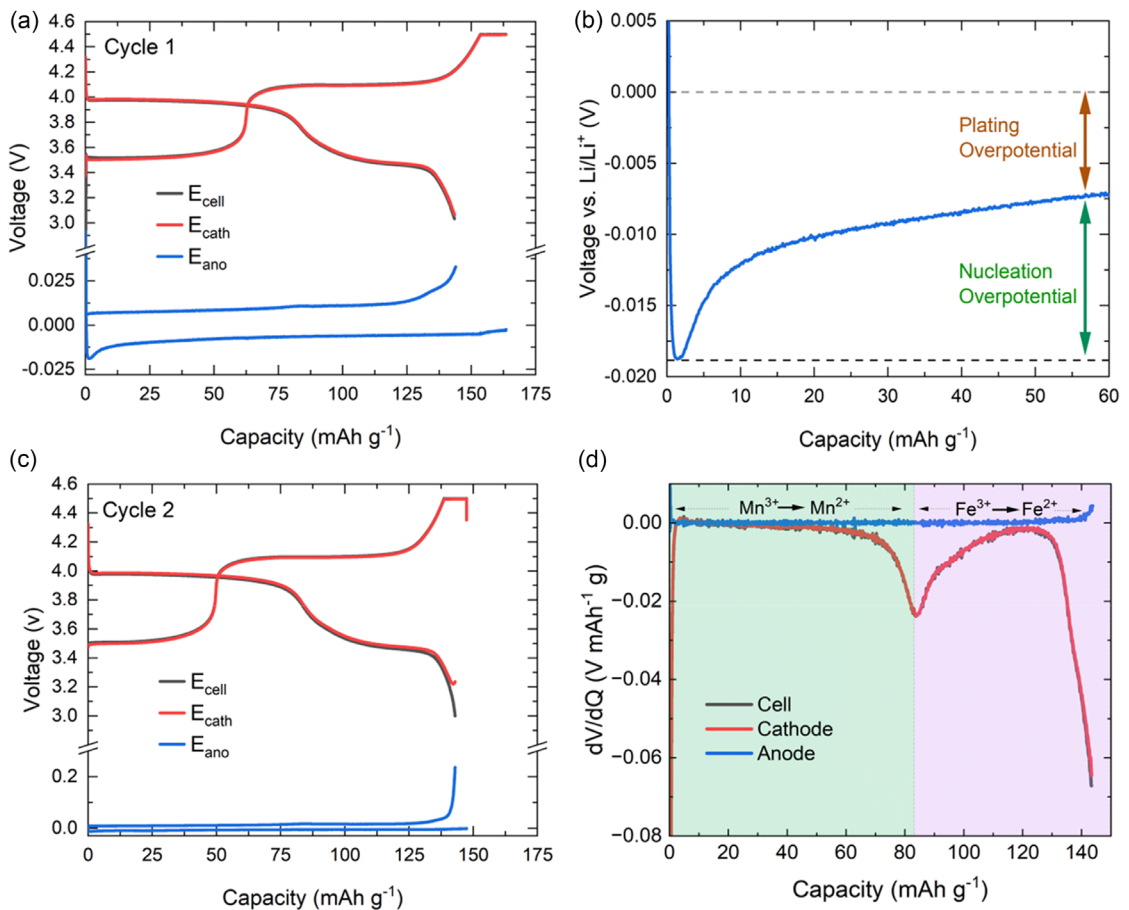


**Figure 2.** 3-electrode cell testing of LMFP AF cell. a,b) Cathode, anode, and cell voltage profiles during cycle 1 and c) cycle 2. d) Differential voltage curves during cycle 1 discharge.

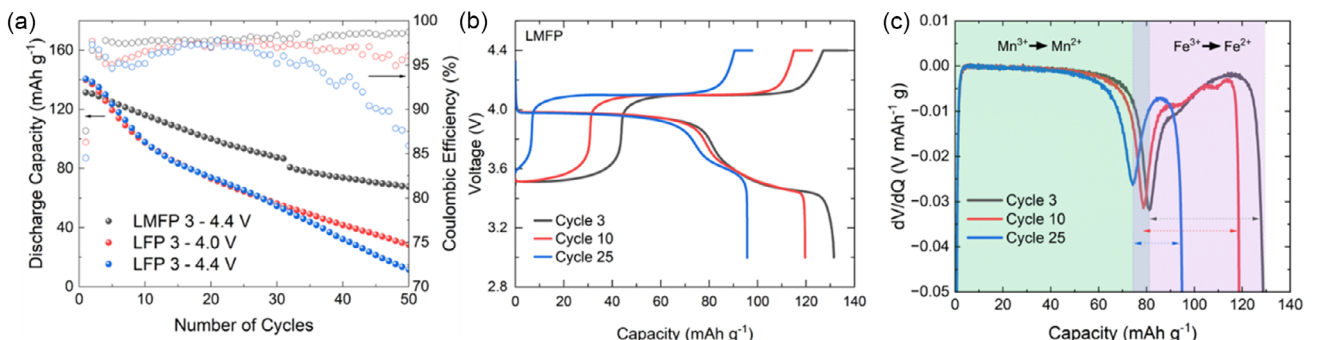


**Figure 3.** a) Discharge capacity and coulombic efficiency of LMFP and LFP AF coin cells during repeated cycling at C/10 and D/3. b) Voltage profiles and c) DVA of selected cycles.

the LMFP AF cell underwent significant capacity loss itself, falling to 68 mAh g<sup>-1</sup> after 50 cycles. The degradation mechanism(s) were further investigated through analysis of the voltage profiles during ageing (Figure 3b). The capacity loss occurred largely in the low voltage (Fe redox) region and was therefore attributed to Li inventory loss. This effect is more difficult to identify with LFP, as only one plateau is present (Figure S2, Supporting Information), however the small amount of low voltage discharge

capacity in the region 3.0–3.3 V visible during cycle 1 had disappeared during cycle 10, and thus the dominant degradation mechanism for both materials was identified as Li inventory loss. Notably, there was little observed shift in plateau potential during ageing, and thus kinetic issues did not appear to play a significant role. DVA of the LMFP cell (Figure 3c) enable better quantification of the relative contribution of Fe & Mn redox processes. During cycle 1, the Fe plateau (the capacity to the right of the peak)

represents 41% of discharge capacity, in line with the 40:60 Fe:Mn content in the pristine material. During cycle 25, the Fe plateau contributed only 22% of capacity. An additional degradation mechanism visible for the LMFP AF cell is voltage decay, whereby the discharge voltage falls in the region 70–80 mAh g<sup>-1</sup> (visible in both the profile in Figure 3b and the shift/broadening of the peak in Figure 3c). This effect, which negatively affects cell energy (but not specific capacity) has been attributed to the buildup of particle and electrode-level heterogeneity with cycling.<sup>[31,32]</sup>

The sources of this inventory loss are common to all AF cells and can be ascribed to both irreversible Li consumption in SEI formation which does not terminate during formation cycling (as fresh Li surfaces are created during each charge cycle), and the creation of “dead” Li, i.e., elemental Li which has become disconnected from the current collector. The morphology of the plated Li is the key driver for these effects; here this was analyzed via cross-sectional scanning electron microscopy (SEM) milling and imaging (under low temperature “cryo” conditions) of anodes harvested from LMFP AF coin cells after the first and 10th charging processes, shown in Figure 4. After the first charge (Figure 4a), the Li exhibited a dense film morphology (albeit with a rough top surface) of thickness in the range 2–11 µm. The dense morphology is advantageous due to both the low surface area (limiting SEI formation) and strong connection to the current collector. Time of flight secondary ion mass spectroscopy (TOF-SIMS) mapping (Figure 4b) was utilized to reveal electrode composition, shown are the maps of the Li<sup>+</sup> and F<sup>-</sup> ions within a selected electrode area. The increased Li<sup>+</sup> signal at grain boundaries and at the surface, compared to elemental Li areas, correlates with locations where the formation of SEI is expected. There, the Li present in ionic form, e.g., LiF, Li<sub>2</sub>CO<sub>3</sub> which, in combination with greater

roughness, likely leads to higher ionization rates and therefore more pronounced SIMS signal. The similar areas in which the fluoride anion was detected further reinforce this conclusion. Notably, despite the dense nature of the film, there is a clear grain structure which appears to be separated by thin regions of SEI. After the 10th charge (Figure 4c), the Li deposition has taken on a much-altered morphology. While there are still large Li grains present, they are spatially separated from one another, increasing both surface area and the likelihood of material becoming disconnected from the current collector. Alongside the large Li grains, much more “mossy” material is visible, likely to be a combination of accumulated SEI, active and inactive Li. Here the SIMS maps reveal the strong presence of SEI on the surface of the large grains and within the mossy regions. This SEI acts both as a cause of Li inventory loss, and likely (with further growth) a resistive barrier, blocking ionic and electronic diffusion within the electrode. Indeed, electrochemical impedance spectroscopy (EIS) spectra of an LMFP AF cell obtained in the pristine and aged states (Figure S3, Supporting Information) reveal a dramatic increase in cell impedance. Strategies to improve the lifetime of AF cells must avoid this disadvantageous evolution in plating morphology. The importance of cross-sectional imaging is highlighted when more straightforward top-down imaging was performed (Figure S4, Supporting Information). Here, only the top layer of Li is observable, and gives the impression of a purely porous morphology, even after just the first charge. The evolution in morphology after 10 cycles is also unclear in top-down view and reinforces the value of the cryo-pFIB cross-sectioning approach.

Li loss via unstable SEI growth is well-established to be exacerbated by the presence of transition metal ions which have

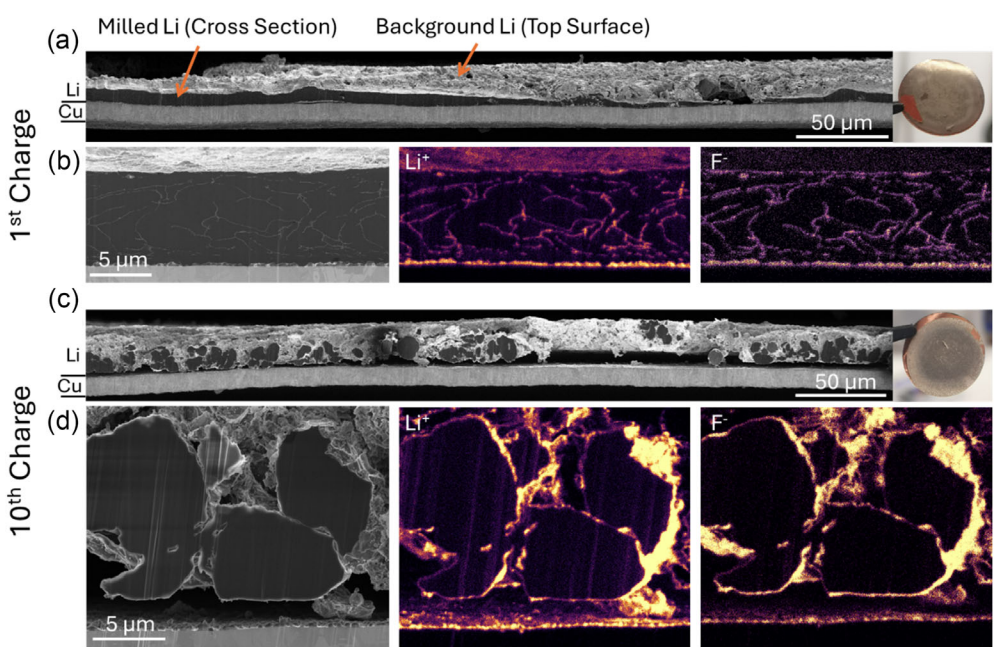


**Figure 4.** Cross-sectional SEM images (milled via cryo-pFIB) and TOF-SIMS maps of Li electrodes harvested from cycled LMFP AF cells cycled at 3–4.4 V. Milled regions of Li electrodes after a) 1st charge cycle and c) Wavelength 10th charge cycle. Inset are photographs of the electrodes taken immediately after cell disassembly. b,d) show images and Li<sup>+</sup>/F<sup>-</sup> signals from selected areas of the electrodes.

dissolved from the cathode and traveled to the anode.<sup>[26,33]</sup> To assess this process, X-ray fluorescence (XRF) was performed on the aged anode (Figure S5, Supporting Information), in which Fe was detected but Mn was not (likely below the detection limit). The generally low TM signals were attributed firstly to the nature of the AF cell type whereby the anode is completely removed and reformed every cycle. This would likely promote the detachment of any TM-containing SEI/dead Li (subsequently washed away during electrode rinsing). Second, TM dissolution may be limited by the relatively small number of cycles (10) over a short time-frame ( $\approx 1$  week). Anodes extracted from cells aged for longer (100 cycles) for the same purpose completely delaminated during disassembly thus preventing SIMS/XRF analysis.

The formation and cycling protocols selected for cell cycling play a dramatic role in determining measured lifetime, particularly so in the case of the AF chemistry.<sup>[23,34]</sup> Here, to maximize the lifetime of the LMFP AF cell, both UCV and LCV were varied, and the effect on capacity monitored. In general, UCV must be sufficiently high to encompass desired electrochemical activity and maximise capacity, but not so high as to induce excess electrolyte decomposition or transition metal dissolution. LMFP AF cells with UCVs in the range 4.2–4.6 V exhibited similar initial capacities in the range 141–144 mAh g<sup>-1</sup> (Figure 5a), indicating that little usable capacity was available in this range (consistent with the presumed termination of Mn redox activity at  $\approx 4.2$  V vs. Li<sup>+</sup>/Li). However, the capacity loss trends were remarkably different for each voltage range, whereby a UCV of 4.5 V resulted in the greatest capacity retention. This UCV maintained the highest coulombic efficiency (CE, Figure 5b) which can be correlated with the lowest rate of Li inventory loss, and thus the longest cell lifetime.

Figure 5c shows the voltage profiles for each UCV during the first cycle. Here the charge capacity exhibited a trend with UCV, 167 mAh g<sup>-1</sup> at 4.6 V to 159 mAh g<sup>-1</sup> at 4.2 V. As noted above, the discharge capacities do not show this trend, with all cells providing similar capacity. The voltage profiles at cycle 25 (Figure S6a) reveal the plateaus have not significantly shifted in potential, indicating that cell polarization has not increased dramatically, and can be ruled out as a major degradation mechanism. For all cells, the Fe plateau has disappeared or dramatically reduced in length, confirming Li inventory loss as the major contributor to capacity loss in all cases.

Given that the major degradation mechanism is Li inventory loss, the question remains as to why it is rather heavily dependent on UCV. A similar effect was previously reported for NMC cathodes.<sup>[35]</sup> Consideration of the mechanics of the first cycle, and the state of the cell at the end of the first cycle, may provide insights. It was noted above that the first cycle charge capacity trended higher with UCV while the discharge capacities were quite similar. It was also established (from 3-electrode cell testing above) that the first cycle discharge is cathode-limited. This implies that a quantity of elemental Li remains on the anode side at the end of discharge, and that this quantity is greater at higher UCV. This reservoir of Li provides an ideal lithiophilic surface for subsequent deposition, aiding in the formation of dense, low surface area films free from dendrites.<sup>[23]</sup> A further increase of UCV of 4.6 V, however, results in more rapid capacity loss, attributed to the dominance of electrolyte decomposition at this potential.

The desirable outcome, i.e., the presence of a Li reservoir on the anode at the end of the first cycle, can also be engineered through modulation of LCV. Here, four LCVs were selected:

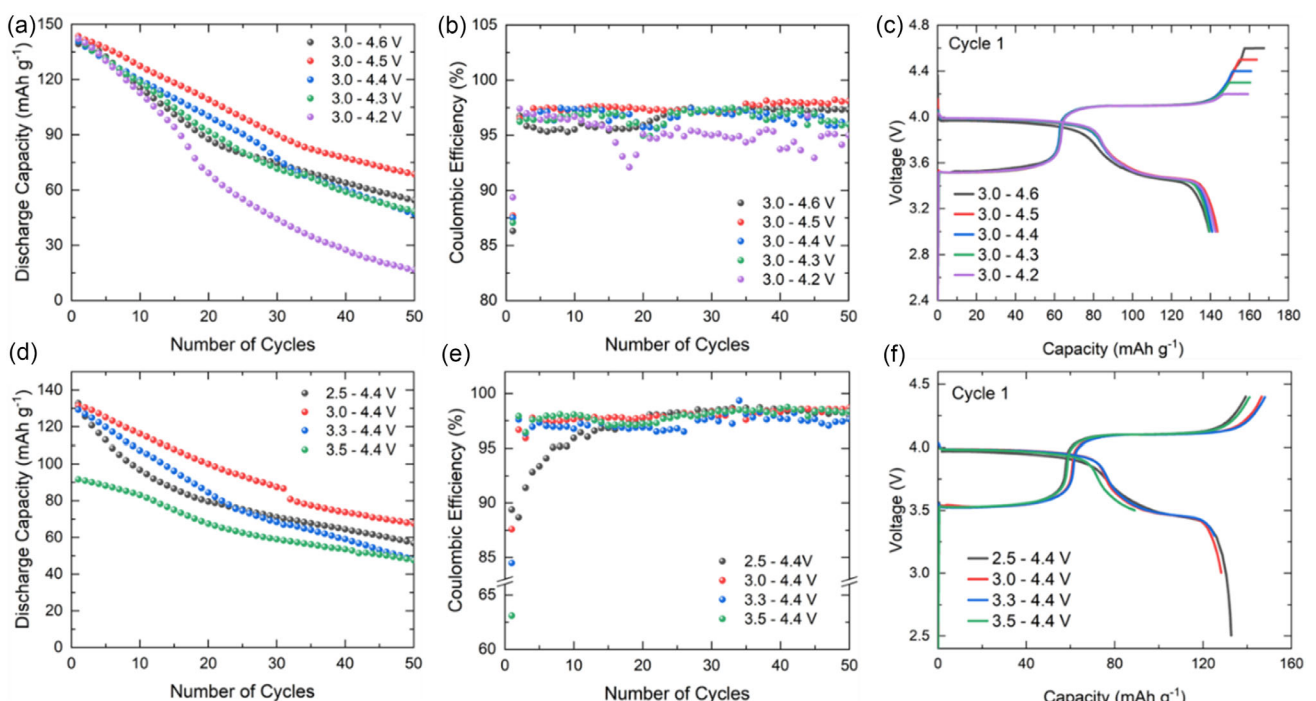


**Figure 5.** Optimization of upper and lower cutoff voltages for LMFP60 AF cells. a) Capacity retention, b) Coulombic efficiency, and c) Cycle 1 voltage profiles as a function of UCV. d) Capacity retention, e) Coulombic efficiency, and f) Cycle 1 voltage profiles as a function of LCV.

2.5 V (expected to encompass all activity), 3.0, 3.3, and 3.5 V (leaving increasing quantities of Li on the Cu surface at the end of discharge). The UCV was held constant at 4.4 V. LCVs of 2.5, 3.0, and 3.3 V had a small effect on initial discharge capacity with values of 132.7, 131.5, and 129.2 mAh g<sup>-1</sup>, respectively, while an LCV of 3.5 V severely reduced capacity to 91.6 mAh g<sup>-1</sup>. Repeated cycling (Figure 5d) revealed that an LCV of 3.0 V resulted in the greatest capacity throughout 50 cycles. The benefits of the

maintenance of a Li reservoir on the anode are clear from the coulombic efficiencies (Figure 5e), whereby discharging all the way to 2.5 V resulted in the highest CE initially, but the lowest thereafter ( $\leq 95\%$  during the first 10 cycles). The initial voltage profiles (Figure 5f) of all cells during discharge tracked one another closely until their cutoff is reached. The cutoff of 3.5 V effectively eliminated most of the Fe redox plateau and thus reduced capacity by 30%. The profiles of cycle 25 (Figure S6) reveal that, unlike the others, the 3.0 V LCV maintains some Fe redox activity (visible in the early stage of charge and later stage of discharge) and thereby achieves the highest capacity at that point.

While testing in coin cell format is rapid and useful for initial performance evaluation and protocol optimization, this format is not commercially relevant for most applications and moreover may obscure certain challenges. For example, coin cells typically utilize a large mass of electrolyte ( $\approx 30 \text{ g Ah}^{-1}$  in the cells studied in this work, compared with  $2\text{--}3 \text{ g Ah}^{-1}$  in commercial formats) which may artificially boost performance due to an excess of SEI-forming additives. Additionally, the small size of coin cells likely leads to significant edge effects, unrepresented in larger cell formats. To demonstrate the scalability of the cell manufacturing

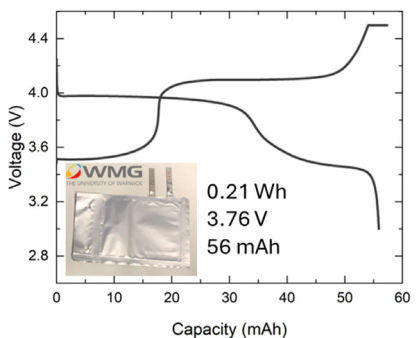


Figure 6. Voltage profile of AF LMFP pouch cell.

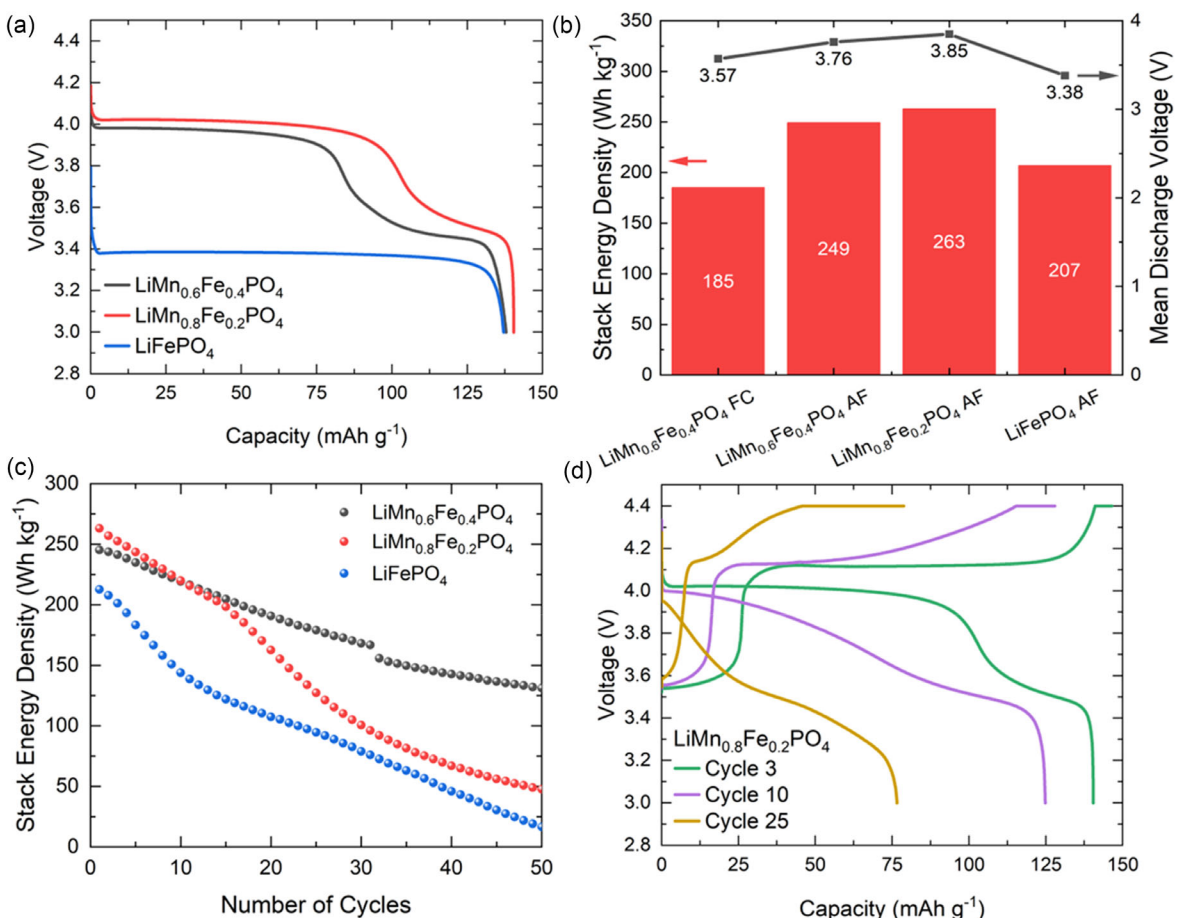


Figure 7. The effect of Mn content in LMFP. a) Voltage profile (1st formation cycle) for LFP and LMFP with Mn contents of 60% and 80%. b) Stack-level energy density and average discharge voltage for four cell types: LMFP FC, LMFP AF, LMFP AF (high Mn content), and LFP AF. c) Repeated cycling, showing stack-level energy density as a function of cycle number. d) Voltage profiles for LiMn<sub>0.8</sub>Fe<sub>0.2</sub>PO<sub>4</sub> for cycles 3, 10, and 25.

showcased in this work, a large area ( $35\text{ cm}^2$  electrode area) AF LMFP pouch cell was manufactured in WMG's battery pilot line facility (**Figure 6**). The cell exhibited a total energy of  $0.21\text{ Wh}$  at an average discharge potential of  $3.76\text{ V}$ . The initial specific capacity ( $137\text{ mAh g}^{-1}$ , Figure S7, Supporting Information) was slightly lower than equivalent coin cells, attributed to the reasons mentioned above. Notably, pouch cell format also enables more direct and accurate control over cell stack pressure, a critical aspect for all forms of Li-metal battery.<sup>[5]</sup>

The introduction of Mn to traditional LFP olivine cathodes unlocks a new degree of freedom for cathode optimization, namely the Mn/Fe ratio. Higher Mn content will result in a greater energy density due to the elevated average voltage and is thus quite desirable. However, this is typically thought to come at the cost of shorter cell lifetime (more Mn dissolution) and poorer kinetics.<sup>[18]</sup> As a compromise, researchers and manufacturers have thus settled on an optimized Mn content in the range 50%–80%.<sup>[8]</sup> To evaluate the effect of (and optimize) this parameter for the AF system, we manufactured similar AF cells to the above, utilizing an LMFP material with 80% Mn ( $\text{LiMn}_{0.8}\text{Fe}_{0.2}\text{PO}_4$ ), and compared with the 60% variant along with LFP. **Figure 7a** shows discharge profiles for these three cells during the first cycle. While all three cells exhibited a similar initial gravimetric capacity in the range  $137\text{--}140\text{ mAh g}^{-1}$ , the advantage to the higher Mn content is clear. The high voltage plateau associated with Mn redox was extended, and the mean discharge voltage increased from  $3.76\text{ V}$  to  $3.85\text{ V}$  (Figure 7b). This in turn increased the stack-level energy by 6% (from  $249\text{ to }263\text{ Wh kg}^{-1}$ ). This compares very favorably with the measured values for the LMFP\Gr FC ( $185\text{ Wh kg}^{-1}$ ) and LFP AF cell ( $207\text{ Wh kg}^{-1}$ ).

This benefit was, however, short-lived. As the cells were cycled repeatedly ( $3.0\text{--}4.4\text{ V}$ , Figure 7c),  $\text{LiMn}_{0.8}\text{Fe}_{0.2}\text{PO}_4$  experienced a more rapid capacity fade, and by cycle 11  $\text{LiMn}_{0.6}\text{Fe}_{0.4}\text{PO}_4$  provided greater energy density. The degradation mechanism(s) were studied in greater detail through observation of the voltage profile during cycling (Figure 7d). Here the poorer kinetics associated with higher Mn content is visible. At cycle 10, the simple two flat plateau arrangement of cycle 1 has been replaced by a gradual sloped charge profile at high SOC. This is reflective of worsening kinetics during charging due to the creation of more Jahn-Teller active  $\text{Mn}^{3+}$ . While this phenomenon occurs in lower Mn content LMFP, it appears likely that the higher Fe content is better able to stabilize the cathode and mitigate undesirable structural evolution. By cycle 25, the profile exhibited large polarization, with the cell hitting the UCV quite early in the charge cycle. This data confirms that increasing the Mn content of LMFP is a viable route to achieving even higher AF energy densities, however the combination of excess Li loss (associated with the AF format coupled with Mn dissolution) and poor kinetics (high Mn content) leads to excessively rapid capacity loss. It is likely that more appropriate electrolyte selection (capable of stabilizing both high Mn LMFP and plated Li) and cathode design (nanosizing, doping) are practical routes to overcoming these challenges.

### 3. Conclusions

In this work, the potential of the AF LMFP system has been evaluated and compared with the traditional full cell format. This proposed configuration has multiple advantages over full cells, boosting energy density through reducing stack mass while significantly simplifying the manufacturing process and reducing cost. This configuration is however noted for poor cycling stability, a challenge which was also highlighted here. The key findings were as follows: 1) Utilizing an LMFP material with 60% Mn, the AF configuration provided a 35% boost to energy density through the removal of the anode host material. 2) Capacity retention of the LMFP cell compared favorably with a similar Mn-free LFP cell, however is still far short of traditional full cells. 3) Li inventory loss was identified as the major capacity loss mechanism through DVA. 4) Variation of the test protocol (specifically UCV and LCV) significantly affected cell degradation characteristics. A cycling range of  $3.0\text{--}4.5\text{ V}$  was found to be optimum, with the UCV sufficiently high to encompass all electrochemical activity while the LCV was suitable to maintain a constant reservoir of Li on the anode side. 5) The simplified manufacturing process for AF cells enabled the scaling of production to pouch cell format, with a  $0.2\text{ Wh}$  cell assembled. 6) Finally, utilizing a higher Mn of 80% provided a further enhancement to energy density, at the cost of more rapid capacity loss associated with more Mn dissolution and worse kinetics.

The surprisingly better lifetime exhibited by LMFP compared with LFP is particularly notable and further investigation is warranted. It is expected that further optimization of electrolyte (tailored for the LMFP AF system) and stack pressure will enable greater cell stability.

### 4. Experimental Section

#### Electrode Preparation

LMFP and graphite electrodes were prepared in WMG's battery scale-up pilot line. Cathode active material ( $\text{LiMn}_{0.6}\text{Fe}_{0.4}\text{PO}_4$  and  $\text{LiFePO}_4$  purchased from Gelon LIB,  $\text{LiMn}_{0.8}\text{Fe}_{0.2}\text{PO}_4$  purchased from ALEES) were mixed with Solef 5130 polyvinylidene (PVDF) and Imerys carbon black C65, in an Eirich EL01 1 L high shear mixer, at a ratio of 93:3.5:3.5 LMFP:PVDF:CB. N-methyl pyrrolidinone (NMP) was added during mixing to a final solid content of 46%. For full cell comparison, an anode active material (graphite purchased from BTR) was mixed with carboxymethyl cellulose (CMC), styrene-butadiene rubber (SBR) and CB at a ratio of Graphite:CMC:SBR:CB 95.25:1.5:2.25:1. De-ionized water was added during mixing to achieve a final solid content of 55%. The slurries were coated onto carbon-coated Al ( $13\text{ }\mu\text{m}$ , Cambridge Energy Solutions) and Cu ( $8\text{ }\mu\text{m}$ , Avocet) foils, for cathode and anode, respectively, on a Megtec reverse comma bar roll-to-roll coating system, to desired coat weights of  $13.5\text{ mg cm}^{-2}$  (LMFP/LFP) and  $7.4\text{ g cm}^{-2}$  (graphite). For LMFP, the coating line was run at a speed of  $0.8\text{ m min}^{-1}$  with drying temperatures of 100, 110, and  $120^\circ\text{C}$  (three zones), and a total area of  $20\text{ m} \times 10\text{ cm}$  was produced. For anode, the speed was  $1.0\text{ m min}^{-1}$  and all three drying zones were set to  $40^\circ\text{C}$ . A total area of  $25\text{ m} \times 10\text{ cm}$  was coated. Electrodes were calendered to densities of  $2.15\text{ g cm}^{-3}$  (LMFP) and  $1.4\text{ g cm}^{-3}$  (Graphite).

## Cell Assembly

For 2032 coin cells, electrode discs were punched to diameters of 14.8 mm (cathode) and 15 mm (anode). Prior to assembly of AF cells, the Cu foil was wiped with de-ionized water and acetone but was otherwise unmodified. Cell assembly was carried out in an Argon-filled glovebox using a Celgard 2325 separator (16 mm diameter), and 100  $\mu$ l electrolyte (0.6 M LiBF<sub>4</sub> + 0.6 M LiDFOB in 1:2 FEC:DEC). 3-electrode "PAT" cells were purchased from EL-cell and assembled in a similar manner with 18 mm diameter electrodes, utilizing a glass fiber separator. Single-layer pouch cell assembly was carried out in a dry room environment (dewpoint  $<-50^{\circ}\text{C}$ ). First, cathodes and anodes were punched to sizes of 4.8  $\times$  6.8 cm (32.6 cm<sup>2</sup>) and 5  $\times$  7 cm (35 cm<sup>2</sup>), respectively. Tags were then welded to enable external connection, before the electrodes were assembled with Celgard 2325 separator into a stack and placed inside the laminated Al pouch. 1 g electrolyte was added, and the cell was sealed at 50 mbar.

## Electrochemical Analysis

All cells were subjected to a 10-hour wetting period at open circuit prior to cycling. Electrochemical testing was carried out using a Biologic BCS cycler (coin and pouch cells) and VMP3 cycler (3-electrode cells). Two formation cycles (C/10, D/3) were performed, followed by EIS. During EIS, a 10 mV amplitude AC voltage signal was applied over the frequency range 10 kHz to 10 mHz. During subsequent cycling (C/10, D/3), a constant-current-constant-voltage (CCCV) charging strategy was employed, whereby the CV step terminated when current reached 10% of that during the CC stage.

## Material Analysis

SEM was conducted at WMG's microscopy suite. For cross-sectional imaging, parts of the Li-plated Cu discs were mounted foil facing up and with a slight overhang of the center region. Mounted samples were Au-coated in an Ar-based coater, housed inside an Ar-filled glove box. The samples were transferred, air protected inside a CleanConnect system, to the Thermo Scientific Helios 5 Hydra plasma focused ion beam (PFIB) SEM. The stage was cooled to  $-150^{\circ}\text{C}$  and held at cryo temperatures throughout milling and imaging. Wide cross-sections were milled with an Ar ion beam at 30 kV, 0.12  $\mu\text{A}$ . After imaging to establish the continuity of the Li-plating of these wide sections, areas were further polished at 30 kV, 7.6 nA for morphological and analytical characterization. Images were collected at 2 kV 0.2 nA with the through lense detector (TLD). ToF-SIMS maps were collected with an Ar beam at 30 kV and a beam current of 60 pA. Images of the surface of the plated Li were collected at room temperature with same beam conditions as above.

Wavelength-dispersive X-ray fluorescence (WD-XRF) spectroscopy was conducted at the University of Warwick X-ray Diffraction Research Technology Platform (RTP) using a Rigaku Primus IV system, equipped with a 4 kW Rh tube. A selection of proprietary monochromators of the Rigaku filters the broader Rh spectrum of X-rays to select a specific wavelength of interest (transition metals). Internal calibration procedures ensure the accuracy of the crystal analyzers (monochromators) and the intensity measurements of the spectrum used in this manuscript.

## Acknowledgements

This work was supported by the Faraday Institution (grant nos. FIRG082, FIRG088). The authors would like to acknowledge

WMG's Battery Scale Up facility team, led by Dr Ieuan Ellis, for their assistance in cell manufacturing, as well as the technical support team led by Shaun Dixon. The authors would also like to acknowledge the support of ThermoFisher Scientific who aided in the establishing of the cryo-pFIB milling and imaging system.

## Conflicts of Interest

The authors declare no conflict of interest.

## Author Contributions

**Gerard Bree:** conceptualization (lead); data curation (lead); formal analysis (lead); investigation (lead); methodology (lead); project administration (supporting); supervision (supporting); validation (lead); visualization (lead); writing—original draft (lead); writing—review & editing (lead). **Daniela Proprentner:** formal analysis (supporting); investigation (supporting); methodology (supporting); visualization (supporting); writing—review & editing (supporting). **Galo Paez-Fajardo:** data curation (supporting); formal analysis (supporting); investigation (supporting); methodology (supporting); writing—review & editing (supporting). **Eleni Fiamiegkou:** investigation (supporting); methodology (supporting). **Veronika Majherova:** investigation (supporting); methodology (supporting). **Louis Piper:** conceptualization (supporting); funding acquisition (lead); project administration (lead); supervision (lead).

## Data Availability Statement

The data that support the findings of this study are available from the corresponding author upon reasonable request.

**Keywords:** anodefree • anodeless • lithium-ion battery • LiMn<sub>x</sub>Fe<sub>1-x</sub>PO<sub>4</sub> • pouch cell

- [1] X. Shen, H. Liu, X.-B. Cheng, C. Yan, J.-Q. Huang, *Energy Storage Mater.* **2018**, *12*, 161.
- [2] B. Acebedo, M. C. Morant-Miñana, E. Gonzalo, I. R. de Larramendi, A. Villaverde, J. Rikarte, L. Fallarino, *Adv. Energy Mater.* **2023**, *13*, 202203744.
- [3] Y. Zhang, T.-T. Zuo, J. Popovic, K. Lim, Y.-X. Yin, J. Maier, Y.-G. Guo, *Mater. Today* **2020**, *33*, 56.
- [4] R. V. Salvatierra, W. Chen, J. M. Tour, *Adv. Energy Sustainability Res.* **2021**, *2*, 202000110.
- [5] A. J. Louli, M. Genovese, R. Weber, S. G. Hames, E. R. Logan, J. R. Dahn, *J. Electrochem. Soc.* **2019**, *166*, A1291.
- [6] C. Soulén, N. Lam, J. Holoubek, P. Liu, *J. Electrochem. Soc.* **2024**, *171*, 2731.
- [7] U. A. P. Centre, *Battery Insight Report—2025 and Beyond: Promising Battery Cell Innovations for the UK Automotive Sector*, **2024**.
- [8] G. Bree, J. Zhao, V. Majherova, D. Proprentner, G. J. P. Fajardo, L. F. J. Piper, *Energy Fuels* **2025**, *39*, 3683.
- [9] N. S. Cattani, E. Noronha, J. Schmied, M. Frieges, H. Heimes, A. Kampker, *Batteries (Basel.)* **2024**, *10*, 10070252.
- [10] C. Liu, W. Shen, X. Liu, Y. Chen, C. Ding, Q. Huang, *J. Energy Storage* **2023**, *64*, 107175.

- [11] E. I., M. Grohol, C. Veeh, European Commission: Directorate-General for Internal Market, Smes, Study on the Critical Raw Materials for the EU. 2023, Final report. Publications Office of the European Union 2023.
- [12] N. T. Nassar, et al, *Sci. Adv.* **2020**, *6*, eaay8647.
- [13] J. A. Louli, A. ElDesoky, J. deGoyer, M. Coon, C. P. Aiken, Z. Simunovic, M. Metzger, J. R. Dahn *J. Electrochem. Soc.* **2022**, *169*, 040517.
- [14] H. Yu, X. Liu, H. Ma, Q. Zhao, *Sustainable Energy Fuels* **2023**, *7*, 4442.
- [15] T. T., et al Beyene, *J. Electrochem. Soc.* **2019**, *166*, A1501.
- [16] Reuters, "China's CATL to Start Mass Output of M3P Batteries This Year., (accessed November 2024) 2024, Available at: <https://www.reuters.com/technology/chinas-catl-start-mass-production-delivery-m3p-batteries-this-year-2023-03-24/>.
- [17] CleanTechnica, "Gotion Introduces LMFP Battery With Energy Density Of 240 Wh/Kg., (accessed November 2024) 2024, Available at: <https://cleantechnica.com/2023/05/20/gotion-introduces-lmfp-battery-with-energy-density-of-240-wh-kg/>.
- [18] G. Bree, V. Majherova, E. Fiamiegou, S. Moharana, L. F. J. Piper, *J. Electrochem. Soc.* **2025**, *172*, 020526.
- [19] M. Zhou, et al, *ACS Nano* **2024**, *18*, 32959.
- [20] L. Nie, R. Gao, M. Zhang, Y. Zhu, X. Wu, Z. Lao, G. Zhou, *Adv. Energy Mater.* **2023**, *14*, 202302476.
- [21] Z. Lv, M. Li, J. Lin, J. Luo, B. Wu, R. Hong, S. C. Cao, *J. Solid State Electrochem.* **2023**, *28*, 577.
- [22] L. F. J. Piper, N. F. Quackenbush, S. Sallis, D. O. Scanlon, G. W. Watson, K. W. Nam, X.-Q. Yang, K. E. Smith, F. Omenya, N. A. Chernova, M. S. Whittingham, *J. Phys. Chem. C* **2013**, *117*, 10383.
- [23] A. J. Louli, M. Coon, M. Genovese, J. deGoyer, A. ElDesoky, J. R. Dahn, *J. Electrochem. Soc.* **2021**, *168*, abe089.
- [24] S. Y. Jeong, S. Lee, H. Lee, K.-M. Roh, C.-W. Lee, I. Jeong, M. S. Chae, *J. Power Sources* **2025**, *626*, 235755.
- [25] S. Li, H. Zhang, Y. Liu, L. Wang, X. He, *Adv. Funct. Mater.* **2023**, *34*, 202310057.
- [26] K. Leslie, J. Harlow, D. Rathore, K. Tuul, M. Metzger, *J. Electrochem. Soc.* **2024**, *171*, 040520.
- [27] T. Ruan, et al, *Nanoscale* **2019**, *11*, 3933.
- [28] B. Zhang, et al, *J. Energy Chem.* **2025**, *100*, 1.
- [29] J. Qian, et al, *Adv. Funct. Mater.* **2016**, *26*, 7094.
- [30] Z. L. Brown, S. Heiskanen, B. L. Lucht, *J. Electrochem. Soc.* **2019**, *166*, A2523.
- [31] Q. Hu, L. Wang, G. Han, J. Liao, J. Liu, J. Yao, X. He, *Nano Energy* **2024**, *123*, 109422.
- [32] E. Xu, et al, *Adv. Energy Mater.* **2024**, *15*, 202404929.
- [33] Y. Xie, et al, *ACS Sustainable Chem. Eng.* **2024**, *12*, 6529.
- [34] S. Kim, P. N. Didwal, J. Fiates, J. A. Dawson, R. S. Weatherup, M. De Volder, *ACS Energy Lett.* **2024**, *9*, 4753.
- [35] R. Weber, M. Genovese, A. J. Louli, S. Hames, C. Martin, I. G. Hill, J. R. Dahn, *Nat. Energy* **2019**, *4*, 683.
- [36] Y. Liu, Y. Zhao, X. Gong, J. Liu, C. Wu, B. Chen, H. Zhan, *ACS Appl. Energy Mater.* **2025**, *8*, 1830.
- [37] X. Ye, et al, *ACS Appl. Mater. Interfaces* **2022**, *14*, 53788.
- [38] F. Huang, et al, *Adv. Funct. Mater.* **2025**, e10253.
- [39] P. Liang, et al, *Adv. Mater.* **2022**, *34*, e2207361.
- [40] L. Lin, et al, *Energy Storage Mater.* **2022**, *45*, 821.

Manuscript received: July 3, 2025

Revised manuscript received: August 20, 2025

Version of record online: